

Wavelength-Sensitive Photocatalytic Degradation of Methyl Orange in Aqueous Suspension over Iron(III)-doped TiO₂ Nanopowders under UV and Visible Light Irradiation

X. H. Wang,[†] J.-G. Li,[†] H. Kamiyama,^{†,‡} Y. Moriyoshi,[‡] and T. Ishigaki^{*,†}

Advanced Materials Laboratory, National Institute for Materials Science, 1-1 Namiki, Tsukuba, Ibaraki 305-0044, Japan, and Department of Materials Chemistry, Hosei University, Kajino-cho, Koganei-shi, Tokyo 184-8584, Japan

Received: January 5, 2006; In Final Form: February 8, 2006

Well-crystallized iron(III)-doped TiO₂ nanopowders with controlled Fe³⁺ doping concentration and uniform dopant distribution, have been synthesized with plasma oxidative pyrolysis. The photocatalytic reactivity of the synthesized TiO₂ nanopowders with a mean particle size of 50–70 nm was quantified in terms of the degradation rates of methyl orange (MO) in aqueous TiO₂ suspension under UV (mainly 365 and 316 nm) and visible light irradiation (mainly 405 and 436 nm). The photodecomposition of MO over TiO₂ nanopowders followed a distinct two-stage pseudo first order kinetics. Interestingly, the photocatalytic reactivity depends not only on the iron doping concentration but also on the wavelength of the irradiating light. Under UV irradiation, nominally undoped TiO₂ had much higher reactivity than Fe³⁺-doped TiO₂, suggesting that Fe³⁺ doping (> 0.05 at. %) in TiO₂ with a mean particle size of approximately 60 nm was detrimental to the photocatalytic decomposition of methyl orange. Whereas, under visible light irradiation, the Fe³⁺-doped TiO₂ with an intermediate iron doping concentration of ~1 at. % had the highest photocatalytic reactivity due to the narrowing of band gap so that it could effectively absorb the light with longer wavelength. A strategy for improving the photocatalytic reactivity of Fe³⁺-doped TiO₂ used in the visible light region is also proposed.

Introduction

Semiconductor photocatalysis to remedy the problem of chemical waste is a promising approach and has attracted much attention.¹ Of the semiconductors investigated, TiO₂ is the most investigated photocatalyst and has been found to be capable of decomposing a wide variety of organics and inorganics in both liquid^{2–19} and gas phases.^{20–26} The basic principle of semiconductor photocatalysis involves photogenerated electrons and holes migrating to the surface and serving as redox sources that react with adsorbed reactants, leading to the destruction of pollutants. The current bottleneck with photocatalysis lies in its low quantum yield, which depends on the ratio of the surface charge carrier transfer rate to the electron–hole (e[−]–h⁺) recombination rate.

To increase the quantum yield of nanocrystalline photocatalysts, the e[−]–h⁺ recombination rate should be reduced. The introduction of defects through selective metal ion doping has been demonstrated to be an effective approach to separate e[−] and h⁺. For example, Choi et al.²⁷ carried out a systematic study on metal ion doping in quantum-sized (2–4 nm) TiO₂ colloids by measuring their photoreactivities and transient charge carrier recombination dynamics. They found that the presence of metal ion dopants in the TiO₂ crystalline matrix significantly influenced photoreactivity, charge carrier recombination rates, and interfacial electron-transfer rates. Of the 21 metal ion dopants investigated previously in the TiO₂ system, Fe³⁺ at 0.1–0.5 at. % has been found to be the most effective dopant for the conduction band electron reduction of an electron acceptor (CCl₄

dechlorination) and the valence band hole oxidation of an electron donor (CHCl₃ degradation). In other heterogeneous photocatalysis systems, the photocatalytic oxidation of methanol, iron doping at 0.25 or 0.5 at. % in TiO₂ (2–4 nm) was also found to be highly effective in enhancing photocatalytic activity.²⁸ In addition to the optimal doping concentration that quantum-sized TiO₂ colloids have,^{27,28} Zhang et al. found that this concentration was dependent on the particle size, i.e., the larger the particle, the smaller the doping concentration.²⁹

By utilizing the unique characteristics of the RF inductive plasma, specifically, high temperature (3000–10 000 K) and the high cooling rate (~10⁶ K/s), we obtained well-crystallized TiO₂ nanopowders with controlled iron doping concentration and uniform dopant distribution.³⁰ This provided an opportunity for us to investigate the effect of Fe³⁺ dopant concentration on the photocatalytic reactivity of TiO₂ in the decomposition of methyl orange under UV and visible light irradiation. We found that under UV irradiation Fe³⁺ doping in TiO₂ with a mean particle size of 50–70 nm was detrimental to the photocatalytic decomposition of methyl orange. This result can be understood from the particle size effect where the optimal dopant concentration is inversely proportional to the particle size. Interestingly, under visible light irradiation TiO₂ with Fe³⁺ at ~1 at. % had higher efficiency than the nominally undoped TiO₂, suggesting that iron doping at a certain level is a promising way of extending the application of TiO₂ as photocatalyst into the visible light region.

Experimental Section

Synthesis and Characterization of Catalyst. The nominally undoped and iron(III)-doped TiO₂ nanopowders used as photocatalysts in this work were synthesized with plasma oxidative

* Corresponding author: Fax: 81-29-8604701. E-mail: Ishigaki.takamasa@nims.go.jp.

[†] National Institute for Materials Science.

[‡] Hosei University.

pyrolysis,³⁰ which is capable of obtaining bare and iron-doped TiO₂ powders with controlled iron doping concentration and uniform iron ion distribution. The iron content of the TiO₂ powders was measured by an inductively coupled plasma-atomic emission spectroscopy (ICP-AES) method. The valence of iron in TiO₂ was determined by Mössbauer spectroscopy. The nanopowders were examined by transmission electron microscopy/high-resolution transmission electron microscopy (TEM/HR-TEM) (JEM-2000EX, JEOL Ltd., Akishima, Japan). The Brunauer–Emmett–Teller (BET) specific surface area was measured by nitrogen adsorption at 77 K using automatic gas adsorption equipment (Belsorp18, BEL Japan, Inc., Osaka, Japan). Prior to the BET measurements, the powders were degassed at 200 °C for 2 h. The mean particle size of the TiO₂ nanopowders was calculated from the BET specific surface area.

Photocatalytic Evaluation. The photocatalytic activity of the synthesized nanopowders was evaluated by the photocatalytic decomposition of methyl orange (MO) in TiO₂ aqueous suspension under UV and visible light irradiation. Reagent-grade MO was purchased from Wako Pure Chemical Industries, Ltd., Osaka, Japan. It was used as received without further purification. Photocatalytic reactions were carried out in 20-mL brown glass bottles (i.d. 2.35 cm) at room temperature. The UV and visible light were respectively generated by UVF-203S Type A and C light sources (San-Ei Electric Co., Ltd., Osaka, Japan) using a 200 W high-pressure mercury lamp. The UV light mainly has five wavelengths of 300, 316, 365, 405, and 436 nm with an intensity ratio of 40:82:100:39:30. The visible light mainly has two wavelengths of 405 and 436 nm with an intensity ratio of 81:100. Prior to light irradiation, TiO₂ nanopowders were first dispersed ultrasonically for 5 min in the brown glass bottle containing 10 mL of 20 μM methyl orange aqueous solution, and suspension was obtained. 5.0 mg of nanopowders was loaded in each run under UV irradiation. UV light or visible light was introduced through a light fiber to irradiate the suspension under agitation with a magnetic bar. The light intensity was adjusted to ~1 mW/cm² at the level of the suspension surface. The loading of nanopowders was 20 mg in each run under visible light irradiation. To eliminate the effect of heat during irradiation, the brown glass bottle was wrapped with tissue paper soaked with water.

A kinetic study was carried out through a set of experimental runs under UV or visible light irradiation for various periods up to 120 min. The MO concentration in the suspension after light irradiation was determined by the absorbance of MO. The TiO₂ particulates were separated from the suspension by centrifugation at 12 000 rounds/min for 30 min to measure MO concentration after irradiation. The supernatant solution was separated and centrifuged once more to remove the particulates as thoroughly as possible. After the second centrifugation, the final supernatant solution was poured into a quartz cell to measure absorbance with a spectrophotometer (V-570, Jasco, Japan). The relative concentration of methyl orange was determined by comparing the integrated absorbance in a wavelength range of 340–600 nm from UV–vis spectra.

Results

According to the results of TEM/HRTEM, X-ray diffraction (XRD), Raman spectroscopy, and Mössbauer spectroscopy, well-crystallized Fe³⁺-doped TiO₂ nanopowders with controlled iron doping concentration and uniform iron ion distribution could be readily obtained with the novel method of plasma oxidative pyrolysis³⁰ by utilizing the high-temperature and high-cooling-rate features of the RF inductive plasma. No other

TABLE 1: Physical Properties of TiO₂ Photocatalysts Used in This Study^a

powder	$R_{\text{Fe/Ti}}$ (at. %)	$D_{\text{Iron(III)}}$ (at. %)	W_{anatase} (wt %)	S_{BET} (m ² /g)
A	0	0.0085	78.4	29.3
B	0.05	0.052	77.2	24.5
C	0.50	0.44	71.6	28.8
D	1.0	0.91	60.2	30.2
E	2.0	1.84	38.4	23.9
F	3.0	2.77	22.7	25.3
G	5.0	4.26	18.1	21.0
H	10.0	8.66		22.7
I	20.0	16.4		26.7

^a $R_{\text{Fe/Ti}}$: nominal atomic ratio of iron to titanium; $D_{\text{Iron(III)}}$: iron doping concentration (atomic ratio of Fe to Fe and Ti, $R_{\text{Fe/(Fe+Ti)}}$); W_{anatase} : anatase weight component; S_{BET} : BET specific surface area.

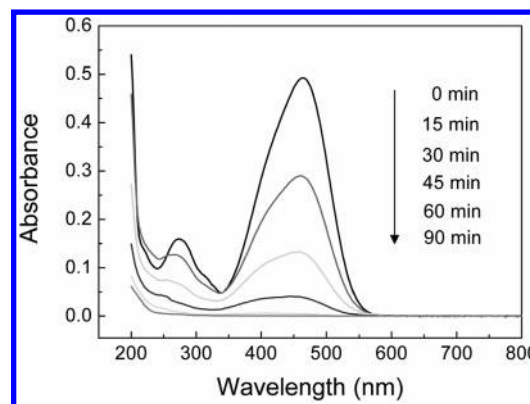


Figure 1. UV-vis absorption spectra for solutions separated from nominally undoped TiO₂ suspensions irradiated for various periods.

phases, except anatase and rutile TiO₂, were identified in the resultant nanopowders due to the very high heating and cooling rate in the liquid-feed plasma oxidative pyrolysis processing. Based on Raman spectroscopy and HRTEM results, iron(III) cations are homogeneously doped in TiO₂ when the nominal atomic ratio of iron to titanium ($R_{\text{Fe/Ti}}$) is below 2%. Above that doping level, excess iron cations are located in the crystallographic shear structure.³⁰ The physical properties of the TiO₂ powders used in this work are summarized in Table 1. The photocatalytic reactivity of the iron-doped TiO₂ nanopowders in the photocatalytic decomposition of an azo dye of methyl orange was evaluated under UV and visible light irradiation.

Under UV Irradiation. When UV light with major wavelengths of 365 and 316 nm irradiated the suspensions containing TiO₂ photocatalysts and methyl orange, a decoloration phenomenon occurred. This suggests that the methyl orange decomposed in the presence of TiO₂ photocatalysts under UV irradiation. To exclude the possibility that the decoloration was caused by the UV itself, we did blank experiments where only methyl orange solution in the absence of TiO₂ photocatalysts was irradiated by UV. The result indicated that the differences in the UV–vis spectra before and after irradiation for various time periods were negligible, indicating that UV light does not decolor MO in the absence of TiO₂ nanopowders.

In the presence of nominally undoped TiO₂, irradiation of the suspension containing MO under UV light resulted in obvious decoloration. This suggests the absorption band of the dye was destroyed during the irradiation. Figure 1 plots the UV–vis spectra for the solutions that were separated from the nominally undoped TiO₂ suspensions irradiated for various periods. It is obvious that the intensity of the absorption band of methyl orange in the visible region decreased significantly

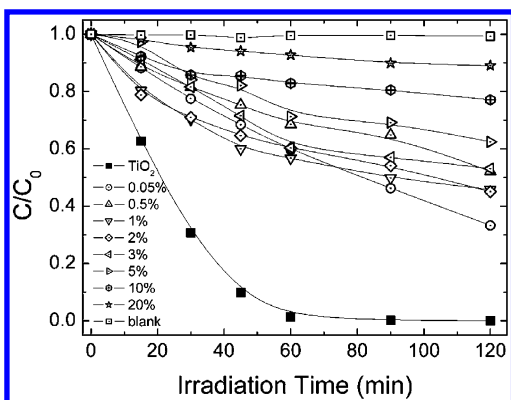


Figure 2. Normalized concentration of methyl orange versus UV irradiation time in the presence of TiO₂ nanopowders with various nominal Fe³⁺ doping concentrations (nominal atomic ratios of Fe to Ti, $R_{\text{Fe/Ti}}$), and in absence of TiO₂ powders. Lines are just guides to the eye.

and monotonically as a function of the irradiation time. This absorption band is completely disappeared after irradiation of 90 min. The dependence of concentration of MO on the irradiation time for the Fe³⁺-doped TiO₂ followed a tendency similar to that of the nominally undoped TiO₂.

Figure 2 plots the normalized concentration of methyl orange in the presence of nominally undoped and Fe³⁺-doped TiO₂ nanopowders, and in the absence of any photocatalyst as a function of irradiation time. As can readily be seen in Figure 2a, the MO concentration decreases much more rapidly for nominally undoped TiO₂ than that for Fe³⁺-doped TiO₂. This indicates that nominally undoped TiO₂ is the most effective photocatalyst for decomposition of MO in water under UV irradiation. In other words, Fe³⁺ doping in TiO₂ particulates with a mean particle size of 50–70 nm was detrimental. This seems to be inconsistent with the previous reports^{27–29} on the effect of iron doping for the photocatalytic decomposition under UV irradiation if the effect of particle size is neglected. Zhang et al.²⁹ did a systematic study on the role of particle size played in pure and iron-doped nanocrystalline TiO₂ photocatalysts under UV irradiation (wavelength 310–330 nm). They found that particle size was a crucial factor in the dynamics of the electron/hole recombination process. The optimal Fe³⁺ dopant concentration for different particle sizes was identified, and this concentration was found to decrease with the increase in particle size.

The Langmuir–Hinshelwood (L–H) model has been successfully applied to describing the kinetics of the heterogeneous catalysis in gas–solid systems. Al-Ekabi and Serpone extended this model into heterogeneous catalysis of a liquid–solid system.³¹ They recognized two extreme situations in defining the surface coverage, θ , of the semiconductor particle: (i) both the reactant and solvent compete for the same active sites, and (ii) both the reactant and solvent are adsorbed on the surface without competing for the same active sites. According to the L–H model, the rate of a unimolecular surface reaction, R , is proportional to θ and follows eq 1a and 1b, respectively, when the reactant is more strongly adsorbed on the surface than the products:

$$R = -dC/dt = k_r\theta = k_rKC/(1+KC+K_sC_s) \quad (1a)$$

$$R = -dC/dt = k_r\theta = k_rKC/(1+KC) \quad (1b)$$

where C is the concentration of the reactant, t is the time, k_r is the reaction rate constant, θ is the fraction of the surface covered

by the reactant, K is the adsorption coefficient of the reactant, K_s is the adsorption coefficient of the solvent, and C_s is the concentration of the solvent.

Integration of eqs 1a and 1b yields eqs 2a and 2b, respectively:

$$\ln \frac{C_0}{C} + \frac{K}{1+K_sC_s}(C_0-C) = \frac{k_rK}{1+K_sC_s}t \quad (2a)$$

$$\ln \frac{C_0}{C} + K(C_0-C) = k_rKt \quad (2b)$$

where C_0 is the initial concentration of the reactant. Obviously, these two equations are the sum of zero-order and first-order rate equations, and their contribution to the overall reaction depends essentially on the initial concentration. When C_0 is very small, eq 2 can be simplified to eq 3.

$$\ln(C_0/C) = k't \quad (3)$$

where k' is the apparent first-order rate constant. This kinetic model has been successfully applied to various heterogeneous photocatalysis systems, e.g., TiO₂/phenol³¹ and ZnO/Remazol Red RR.³²

Under the conditions of the experiments we used here, the initial concentration of methyl orange, C_0 , is 20 μM , which is very small. The $\ln(C_0/C)$ vs t curves for TiO₂ with various nominal iron doping concentrations are plotted in Figure 3a. The linearity of the curves in two time stages indicates that the kinetics for the photocatalytic decomposition of MO follows a two-stage pseudo first order rate. The rate constant in the first stage for nominally undoped TiO₂ is smaller than that in the second one as can be seen from Figure 3b. For TiO₂ with a very low iron doping concentration (TiO₂, 0.05%), the rate constant in the first stage is almost the same as that in the second stage, whereas for the remaining iron-doped TiO₂, the first-stage rate constants are all greater than those in the second stage, which demonstrates that the photocatalytic decomposition of MO is inhibited. There is a similar inhibiting effect on photooxidation of methyl orange, i.e., dye oxidation obeyed an initial burst followed by slower steady decay, as was observed by Brown and Darwent³³ when they studied the photooxidation of colloidal TiO₂ using methyl orange as a probe molecule. They attributed this inhibiting effect to the surface adsorbed peroxide formed by the reduction of O₂ and the oxidation of surface hydroxyl groups. It has been found that H₂O₂ is chemisorbed onto TiO₂ at low pH to give a surface peroxo complex.³⁴ Due to the establishment of a chemisorbed species such as H₂O₂ in the initial stage, the adsorption site for methyl orange on TiO₂ surfaces decreased, and consequently slower steady decay appeared. For the nominally undoped TiO₂ and that with very low iron doping concentration in the present work, the absence of decay in the rate suggests that they are capable of avoiding the accumulation of H₂O₂ due to their higher photo quantum efficiency. H₂O₂ can be converted into $\cdot\text{OH}$, which is responsible for the photocatalytic oxidation of methyl orange reactive species through absorbing valence-band hole, h_{vb}^+ , generated by UV irradiation.¹⁰

Under Visible Light Irradiation. According to the diffuse reflectance UV–vis spectra,³⁰ iron doping leads to absorption edge shift to the visible light region due to the introduction of the 3d electron state of Fe³⁺, 3d⁵, in the conduction band of TiO₂. This implies that iron-doped TiO₂ may be photocatalytically reactive under visible light irradiation. To check whether this was possible, we carried out a set of experiments using

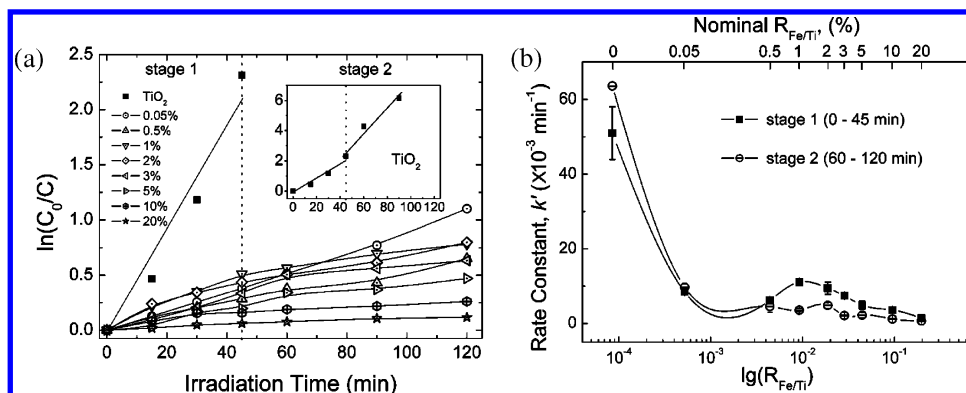


Figure 3. (a) $\ln(C_0/C)$ versus irradiation time for TiO₂ nanopowders with various Fe³⁺ nominal doping concentrations. Inset plots $\ln(C_0/C)$ vs time for nominally undoped TiO₂. Note distinct two-stage pseudo first order kinetics. (b) Pseudo first order rate constants in two stages for TiO₂ nanopowders as function of Fe³⁺ doping concentration. Lines are just guides to the eye.

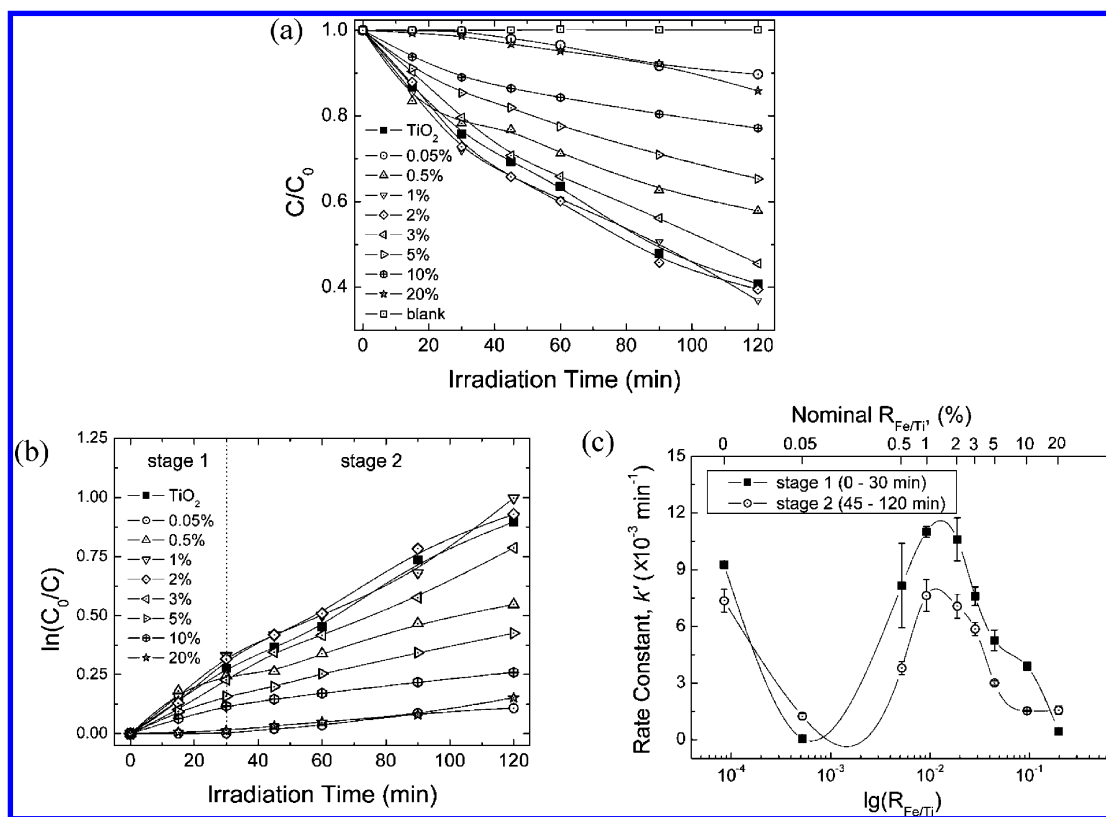


Figure 4. (a) Normalized concentration of methyl orange vs visible light irradiation time in the presence of TiO₂ nanopowders with various Fe³⁺ nominal doping concentration, and in the absence of any TiO₂ powders; (b) $\ln(C_0/C)$ vs time for TiO₂ nanopowders with various Fe³⁺ doping concentration; (c) rate constants in two stages for TiO₂ nanopowders vs Fe³⁺ doping concentration. Lines are just guides to the eye.

iron-doped TiO₂ nanopowders with various iron doping concentrations as photocatalysts. The photocatalytic reactivity of the iron-doped TiO₂ nanopowders was evaluated by the pseudo first order rate constant of the photocatalytic decomposition of methyl orange.

Figure 4a presents the normalized concentration of methyl orange vs irradiation time. Analogous to UV light irradiation, the blank experiment in the absence of TiO₂ revealed that visible light irradiation did not change MO concentration. Thus, the decreased concentrations of MO under visible light irradiation in the presence of TiO₂ originated from the photocatalytic effect of TiO₂. It needs to be noted that all specimens were photocatalytic reactive for the decomposition of MO under visible light irradiation. Moreover, the effect of Fe³⁺ doping concentration on the photocatalytic reactivity is obvious as shown in Figure 4a. Nominally undoped TiO₂ has high reactivity in the decomposition of MO. The nominally undoped TiO₂ contains

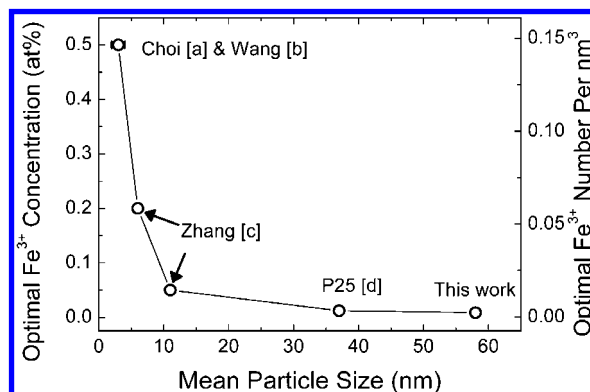
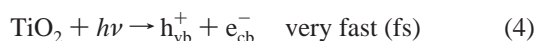


Figure 5. Optimal Fe³⁺ concentration (at. %) and number of Fe³⁺ dopants per cubic nanometer in TiO₂ as a function of particle size under UV irradiation. [a]: ref 27; [b]: ref 28; [c]: ref 29; [d]: ref 38. Lines are just guides to the eye.

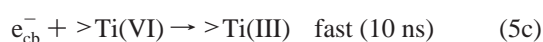
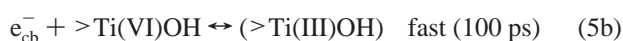
85 ppm iron. The absorption edge shifts to visible light range and thus it is active under visible light irradiation. When even a very small amount of iron was doped, e.g., 0.05 at. % in TiO₂ matrix, the reactivity decreased significantly. Doping with this concentration may only have increased the charge carrier recombination rate due to the large particle size (50–70 nm) in the present work. With a further slight increase in the Fe³⁺ doping concentration, the reactivity reached a peak and was higher than that for the nominally undoped TiO₂. When the doping concentration was excessive, the reactivity degraded monotonically with the increase in Fe³⁺ doping concentration. The reason for the increased reactivity of those nanopowders with moderate Fe³⁺ doping concentrations of ~1 at. % is that the band gap of TiO₂ narrowed in these cases so that they could effectively absorb light with a longer wavelength of 436 nm, while for the nominally undoped TiO₂, that part of light with longer wavelength was not sufficient for charge-carrier generation. At this point, it would be reasonable to conclude that Fe³⁺ doping in TiO₂ extended the absorption of visible light as compared with the relation between pseudo first order rate constants and iron doping concentrations under UV irradiation (Figure 3b). As previously noted, there is an optimal Fe³⁺ doping concentration under UV irradiation. Analogously, there should also be an optimal Fe³⁺ doping concentration for TiO₂ under visible light irradiation.

Discussion

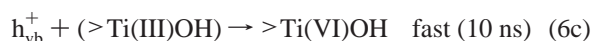
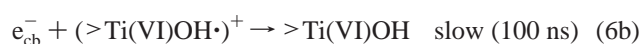
Effect of Particle Size on Photocatalytic Efficiency of Nominally Undoped and Fe³⁺-doped TiO₂. It is generally acknowledged that heterogeneous photocatalysis on TiO₂ involves four processes, i.e., charge-carrier generation, charge-carrier trapping, charge-carrier recombination, and interfacial charge transfer.¹ These are detailed below. Charge-carrier generation:



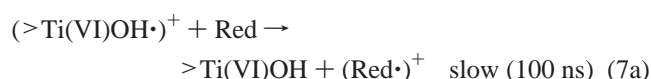
Charge-carrier trapping:



Charge-carrier recombination



Interfacial charge transfer



where $>\text{Ti(VI)OH}$ represents the primary hydrated surface functionality of TiO₂, e_{cb}^- is a conduction-band electron, h_{vb}^+ is a valence-band hole, Red is an electron donor (i.e., reductant),

Ox is an electron acceptor (i.e., oxidant), $(>\text{Ti(VI)OH}\cdot)^+$ is the surface-trapped VB hole (i.e., surface-bound hydroxyl radical), and $(>\text{Ti(III)OH})$ is the surface-trapped CB electron.

According to the mechanism,¹ the overall quantum efficiency for interfacial charge transfer is determined by two critical processes. These are the competition between charge-carrier recombination and trapping followed by the competition between trapped carrier recombination and interfacial charge transfer. An increase in either the recombination lifetime of charge carriers or the interfacial electron-transfer rate is expected to result in higher quantum efficiencies for steady-state photocatalysis.

For pure TiO₂, the charge-carrier recombination may be grouped into volume recombination and surface recombination depending on where the recombination occurs. Volume recombination is dominant in well-crystallized large TiO₂ particles, which can be inhibited through decreasing particle size. A decrease in particle size can also give rise to larger specific surface area, which increases the available surface active sites, and consequently leads to a higher interfacial charge carrier transfer rate for photocatalysis. However, as the semiconductor particle size is too small in the order of several nonometers in diameter, surface recombination becomes an important process.³⁵ In the ultrafine-particle regime, most charge-carriers are generated sufficiently close to the surface. As a result, photogenerated charge carriers may quickly reach the surface and undergo rapid surface recombination, which is mainly due to abundant surface trapping sites and the lack of driving force to separate charge carriers.³⁵ Since the surface carrier recombination is much faster than the interfacial charge carrier transfer process (eqs 6 and 7), the increased interfacial transfer rate is outweighed by the increased surface recombination rate for ultrafine particles smaller than a certain size reduction. Therefore, there is an optimal particle size in the pure TiO₂ system to obtain the highest photocatalytic efficiency.²⁹

There is also an optimal particle size for Fe³⁺-doped TiO₂ to obtain the highest photocatalytic efficiency. For the quantum-sized TiO₂ (2–4 nm), the optimal doping concentration is near 0.5 at. %.^{27,28} With this doping concentration, there is only about one dopant in each particle. Iron doping in the quantum-sized TiO₂ yields two opposite effects. On one hand, an increase in trapping sites through iron doping leads to effective trapping sites for charge carriers, which is a positive effect. On the other hand, the increased number of trapped charge carriers results in shorter lifetimes for interfacial charge transfer, which is a negative effect. Therefore, it is understandable that the appearance of an optimal dopant concentration in quantum-sized TiO₂ is the balance of increased trapping sites, leading to efficient trapping and fewer trapped carriers leading to longer lifetimes for interfacial charge transfer.²⁷ There was an optimal doping concentration for the quantum-sized TiO₂. There should also be an optimal doping concentration for TiO₂ powders with larger particle size, which has been experimentally verified.²⁹ The theoretical work has argued that recombination through tunneling between trapped charge carriers depends on the distance, r , separating the e^- – h^+ pair according to³⁶

$$k_{\text{recomb}} \propto \exp(-2r/a_0) \quad (8)$$

where k_{recomb} is the recombination rate and a_0 is the radius of the hydrogenic wave function of the trapped carriers. It is obvious that the recombination rate increases exponentially with the dopant concentration because the average distance between trap sites decreases with the increasing number of dopants confined within a particle. Alternatively, we should bear in mind

that only charge carriers diffuse to the surface where they undergo chemical reactions with suitable solutes (see the band picture in the reviews in refs 35d and 37). Applying a random walk model to describe the motion of the charge carriers, one obtains the average transit time, τ , from the interior of the particle to the surface as follows:³⁷

$$\tau = (r_0)^2/\pi^2 D \quad (9)$$

where r_0 is the radius of the particle, and D is the diffusion coefficient of the charge carrier. The average transit time is strongly particle-size dependent for TiO₂ nanopowders with a given dopant concentration but a different particle size. The transit time for the smaller particle is shorter and consequently there is less recombination possibility, while for the larger particle, the transit time is much longer and consequently there is more recombination possibility. To make recombination possible for larger particles comparable to smaller ones, recombination centers originating from dopants should be decreased, i.e., decreasing the doping concentration in the larger particles. In combination with the data from the previous works done by the other researchers, we plot the relation between optimal Fe³⁺ concentration (at. %) in TiO₂ and particle size. It is obvious that the optimal Fe³⁺ concentration in TiO₂ decreases with the increase of particle size.

Further Improvements to the Photocatalyst Design through Controlled Iron Doping. The mean particle size of the TiO₂ nanopowders we used as photocatalysts in this work was 50–70 nm. This was larger than that at optimal iron doping concentration under UV irradiation, and therefore the nominally undoped TiO₂ had the highest photocatalytic reactivity. Further improvements to photocatalyst design should be focused on the decrease of particle size of iron-doped TiO₂, which is photocatalytically active in the UV region.

The nanocrystalline TiO₂ catalysts in our study were synthesized by instantaneous high-temperature processing using RF inductive plasma as a reaction zone. Well-crystallized TiO₂ with controlled dopant concentration could readily be produced using this novel method of synthesis. The photoreactivity of the Fe³⁺-doped TiO₂ with an intermediate doping concentration of about 1 at. % is likely to be further improved under visible light irradiation if the particle size is decreased.

Conclusions

The effect of iron doping concentration on the photocatalytic reactivity of well-crystallized Fe³⁺-doped TiO₂ with controlled iron doping concentration ($R_{\text{Fe}/(\text{Fe}+\text{Ti})}$) up to 16.4 at. %, was investigated under UV and visible light irradiation. We found that any Fe³⁺ doping led to a decrease in the photocatalytic decomposition rate of MO under UV irradiation, suggesting that iron doping in TiO₂ with a particle size of 50–70 nm is detrimental. In contrast, under visible light irradiation, TiO₂ with an intermediate iron doping concentration at ~1 at. % had the highest photocatalytic reactivity due to the narrowing of band gap so that it could effectively absorb the light with longer wavelengths. This suggests that iron doping with an optimal concentration holds promise for finding photocatalysts that are active in the visible light region. We also proposed a strategy to further improve the photocatalytic reactivity of iron-doped TiO₂ under visible light irradiation.

Acknowledgment. This work was partly supported by the Industrial Technology Grant Program, contract number ID04A26018, from New Energy and Industrial Technology Development Organization (NEDO), Japan.

References and Notes

- (1) Hoffmann, M. R.; Martin, S. T.; Choi, W.; Bahnemann, D. W. *Chem. Rev.* **1995**, 95, 69 and references therein.
- (2) Alekabi, H.; Serpone, N. *J. Phys. Chem.* **1988**, 92, 5726.
- (3) Prairie, M. R.; Evans, L. R.; Stange, B. M.; Martinez, S. L. *Environ. Sci. Technol.* **1993**, 27, 1776.
- (4) Stafford, U.; Gray, K. A.; Kamat, P. V. *J. Phys. Chem.* **1994**, 98, 6343.
- (5) Martin, S. T.; Lee, A. T.; Hoffmann, M. R. *Environ. Sci. Technol.* **1995**, 29, 2567.
- (6) Schmelling, D. C.; Gray, K. A. *Water Res.* **1995**, 29, 2651.
- (7) Vinodgopal, K.; Wynkoop, D. E.; Kamat, P. V. *Environ. Sci. Technol.* **1996**, 30, 1660.
- (8) Schmelling, D. C.; Gray, K. A.; Kamat, P. V. *Environ. Sci. Technol.* **1996**, 30, 2547.
- (9) Huang, M.; Tso, E.; Datye, A. K.; Prairie, M. R.; Stange, B. M. *Environ. Sci. Technol.* **1996**, 30, 3084.
- (10) Sun, L. Z.; Bolton, J. R. *J. Phys. Chem.* **1996**, 100, 4127.
- (11) Choi, W. Y.; Hoffmann, M. R. *Environ. Sci. Technol.* **1997**, 31, 89.
- (12) Madden, T. H.; Datye, A. K.; Fulton, M.; Prairie, M. R.; Majumdar, S. A.; Stange, B. M. *Environ. Sci. Technol.* **1997**, 31, 3475.
- (13) Andreozzi, R.; Caprio, V.; Insola, A.; Marotta, R. *Catal. Today* **1999**, 53, 51.
- (14) Herrmann, J. *Catal. Today* **1999**, 53, 115.
- (15) Bauer, R.; Waldner, G.; Fallman, H.; Hager, S.; Klare, M.; Krutzler, T.; Malato, S.; Maletzky, P. *Catal. Today* **1999**, 53, 131.
- (16) Cunningham, J.; Al-Sayyed, G.; Sedlak, P.; Caffrey, J. *Catal. Today* **1999**, 53, 145.
- (17) Alfano, O. M.; Bahnemann, D.; Cassano, A. E.; Dillert, R.; Goslich, R. *Catal. Today* **2000**, 58, 199.
- (18) Bhatkhande, D. S.; Pangarkar, V. G.; Beenackers, A. A. C. M. *J. Chem. Technol. Biotechnol.* **2001**, 77, 102.
- (19) Pirkanniemi, K.; Sillanpaa, M. *Chemosphere* **2002**, 48, 1047.
- (20) Jacoby, W. A.; Nimlos, M. R.; Blake, D. M.; Noble, R. D.; Koval, C. A. *Environ. Sci. Technol.* **1994**, 28, 1661.
- (21) Grela, M. A.; Colussi, A. J. *J. Phys. Chem.* **1996**, 100, 10150.
- (22) Muggli, D. S.; Larson, S. A.; Falconer, J. L. *J. Phys. Chem.* **1996**, 100, 15866.
- (23) Sadeghi, M.; Liu, W.; Zhang, T. G.; Stavropoulos, P.; Levy, B. J. *J. Phys. Chem.* **1996**, 100, 19466.
- (24) Ohko, Y.; Tryk, D. A.; Hachimoto, K.; Fujishima, A.; Obee, T. N.; Brown, R. T. *J. Phys. Chem. B* **1998**, 102, 2699.
- (25) Obee, T. N.; Brown, R. T. *Environ. Sci. Technol.* **1995**, 29, 1223.
- (26) Yu, J. C.; Yu, J.; Ho, W.; Jiang, Z.; Zhang, L. *Chem. Mater.* **2002**, 14, 3808.
- (27) Choi, W.; Termin, A.; Hoffmann, M. R. *J. Phys. Chem.* **1994**, 98, 13669.
- (28) Wang, C. Y.; Böttcher, C.; Bahnemann, D. W.; Dohrmann, J. K. *J. Mater. Chem.* **2003**, 13, 2322.
- (29) Zhang, Z.; Wang, C. C.; Zakaria, R.; Ying, J. T. *J. Phys. Chem. B* **1998**, 102, 10871.
- (30) Wang, X. H.; Li, J. G.; Kamiyama, H.; Katada, M.; Ohashi, N.; Moriyoshi, Y.; Ishigaki, T. *J. Am. Chem. Soc.* **2005**, 127, 10982.
- (31) Alekabi, H.; Serpone, N. *J. Phys. Chem.* **1988**, 92, 5726.
- (32) Yatmaz, H. C.; Akyol, A.; Bayramoglu, M. *Ind. Eng. Chem. Res.* **2004**, 43, 6035.
- (33) Brown, G. T.; Darwent, J. R. *J. Phys. Chem.* **1984**, 88, 4955.
- (34) Boonstra, A. H.; Mutsaers, C. A. H. *J. Phys. Chem.* **1975**, 79, 1940.
- (35) (a) Kortan, A. P.; Hull, R.; Opila, R. L.; Bawendi, M. G.; Steigerwald, M. L.; Carroll, P. J.; Brus, L. E. *J. Am. Chem. Soc.* **1990**, 112, 1327. (b) Serpone, N.; Lawless, D.; Khairutdinov, R.; Pelizzetti, E. *J. Phys. Chem.* **1995**, 99, 16655. (c) Hines, M. A.; Guyot-Sionnest, P. *J. Phys. Chem.* **1995**, 100, 468. (d) Linsebigler, A. L.; Lu, G.; Yates, J. T. *Chem. Rev.* **1995**, 95, 735.
- (36) Grätzel, M. *Heterogeneous Photochemical Electron-Transfer Reactions*; CRC Press: Boca Raton, FL, 1987.
- (37) Hagfeldt, A.; Grätzel, M. *Chem. Rev.* **1995**, 95, 49.
- (38) Material data sheet for Degussa P25.